

# Emergence of Negative Capacitance in Multidomain Ferroelectric–Paraelectric Nanocapacitors at Finite Bias

Shusuke Kasamatsu,\* Satoshi Watanabe, Cheol Seong Hwang,\* and Seungwu Han

In order to maintain the shrinking of semiconductor device design rule, an equivalent oxide thickness ( $t_{\text{ox}}$ ) of  $<0.3$  nm will be necessary within the next ten years, especially for nanocapacitors used in dynamic random access memory (DRAM).<sup>[1]</sup> Achieving this for reasonably thick dielectric films to minimize leakage current has proven to be quite challenging, as the dielectric response of higher dielectric constant (i.e., higher- $k$ ) materials such as  $\text{TiO}_2$  and  $\text{SrTiO}_3$  deteriorate rather drastically in thin-film geometries<sup>[2,3]</sup> (experimentally,  $t_{\text{ox}}$  is about 0.38–0.39 nm for a 8.5-nm STO film.<sup>[4]</sup> First-principles simulations have suggested that at least a significant portion of the permittivity decrease is due to intrinsic properties of the metal/dielectric interface (“interfacial dead layer”) and would remain even when perfect epitaxy is achieved.<sup>[5]</sup> This is backed up by experimentally obtained interfacial capacitance values<sup>[3,6,7]</sup> that are comparable to the intrinsic values obtained from first principles.

In order to work around this problem, the use of negative capacitance has gained attention in recent years as an approach to enhancing capacitance density<sup>[8–10]</sup> without further thinning of the dielectric material. Recent experimental works have reported capacitance enhancement due to negative capacitance of 2D electron gas near carrier depletion<sup>[11]</sup> and that of ferroelectric oxide.<sup>[12–16]</sup> Here, we focus on the latter. The emergence of negative capacitance has been explained<sup>[8,12]</sup> by the fact that the energy versus electric displacement curves of ferroelectric materials exhibit negative curvature near zero displacement. Usually, this region is thermodynamically unstable and the ferroelectric would spontaneously polarize. However, it is argued that the polarization can be suppressed by depolarizing

field effects that increase the polarization stiffness. Such an effect can be introduced by placing the ferroelectric in series with a normal positive capacitor, and this normal capacitor can also take the form of the interfacial dielectric dead layer (this is discussed in more detail in the Supporting Information). Indeed, uniform polarization was found to be suppressed in first-principles simulation of metal/ferroelectric/metal capacitors when the ferroelectric was under a critical thickness of the order of a few nanometers.<sup>[17,18]</sup>

However, the above discussion does not take into account the fact that ferroelectrics usually form domains to decrease the depolarization energy. Formation of  $180^\circ$  striped domains can confine the depolarizing field to the surface of the film, allowing the ferroelectric to polarize and lower the energy of the system.<sup>[19–24]</sup> This would severely limit the magnitude of negative capacitance that can be attained.<sup>[25]</sup> However, works on various heterostructures containing ferroelectric thin films have indicated that a clear striped-domain structure does not always occur, and that the ferroelectric domain formation in thin-film geometries depend on the film thickness, boundary condition, and the specific ferroelectric material.<sup>[26–31]</sup> The possibility of domain-motion-induced enhancement of capacitance has also been suggested in the literature.<sup>[12,29,32,33]</sup>

Here, we aim to evaluate the usefulness of ferroelectric negative capacitance focusing on the impact of domain formation in nanodevices. The static dielectric response of the bilayer ferroelectric–paraelectric (FE–PE) nanocapacitor is simulated from first principles utilizing our recently developed orbital-separation approach.<sup>[34]</sup> We employ  $\text{SrRuO}_3$  (SRO) electrodes and STO and  $\text{BaTiO}_3$  (BTO) as the paraelectric and ferroelectric layers, respectively. The striped-multidomain SRO–BTO–STO–SRO capacitor is modeled by a supercell with  $1 \times 4$  in-plane cubic perovskite unit cells shown in **Figure 1a**. The out-of-plane layer stacking can be represented as  $(\text{SrO}-\text{RuO}_2)_{N_{\text{SRO}}}-\text{SrO}-\text{TiO}_2-(\text{BaO}-\text{TiO}_2)_{N_{\text{BTO}}}-(\text{SrO}-\text{TiO}_2)_{N_{\text{STO}}}-\text{SrO}-(\text{RuO}_2-\text{SrO})_{N_{\text{SRO}}}$ , where we have set  $(N_{\text{BTO}}, N_{\text{STO}}) = (3, 6)$ . The electrode thicknesses should be thick enough to screen the interface charge, and we have chosen  $N_{\text{SRO}} = 4$  and  $N_{\text{SRO}'} = 5$  for balance of accuracy and efficiency. We also performed calculations on a supercell with only one in-plane unit cell to constrain the system to be monodomain. It is expected that spontaneous polarization would be suppressed and negative capacitance would be observed in this monodomain-constrained model since  $N_{\text{BTO}} = 3$  is thinner than the critical thickness for uniform polarization<sup>[18]</sup> (to be more precise, the critical thickness was calculated for the SRO–BTO–SRO capacitor in ref. [18]; however, addition of STO layers should basically add to the polarization stiffness unless nothing drastic occurs at the interfaces, so we can expect polarization

Dr. S. Kasamatsu  
The Institute for Solid State Physics  
The University of Tokyo  
5-1-5 Kashiwanoha, Kashiwa-shi, Chiba 277-8581, Japan  
E-mail: kasamatsu@issp.u-tokyo.ac.jp

Prof. S. Watanabe  
Department of Materials Engineering  
The University of Tokyo  
7-3-1 Hongo, Bunkyo-ku, Tokyo 113-8656, Japan

Prof. C. S. Hwang  
Department of Materials Science and Engineering  
and Inter-University Semiconductor Research Center  
Seoul National University  
Seoul 151-742, South Korea  
E-mail: cheolsh@snu.ac.kr

Prof. S. Han  
Department of Materials Science and Engineering  
Seoul National University  
Seoul, 151-742, South Korea



DOI: 10.1002/adma.201502916

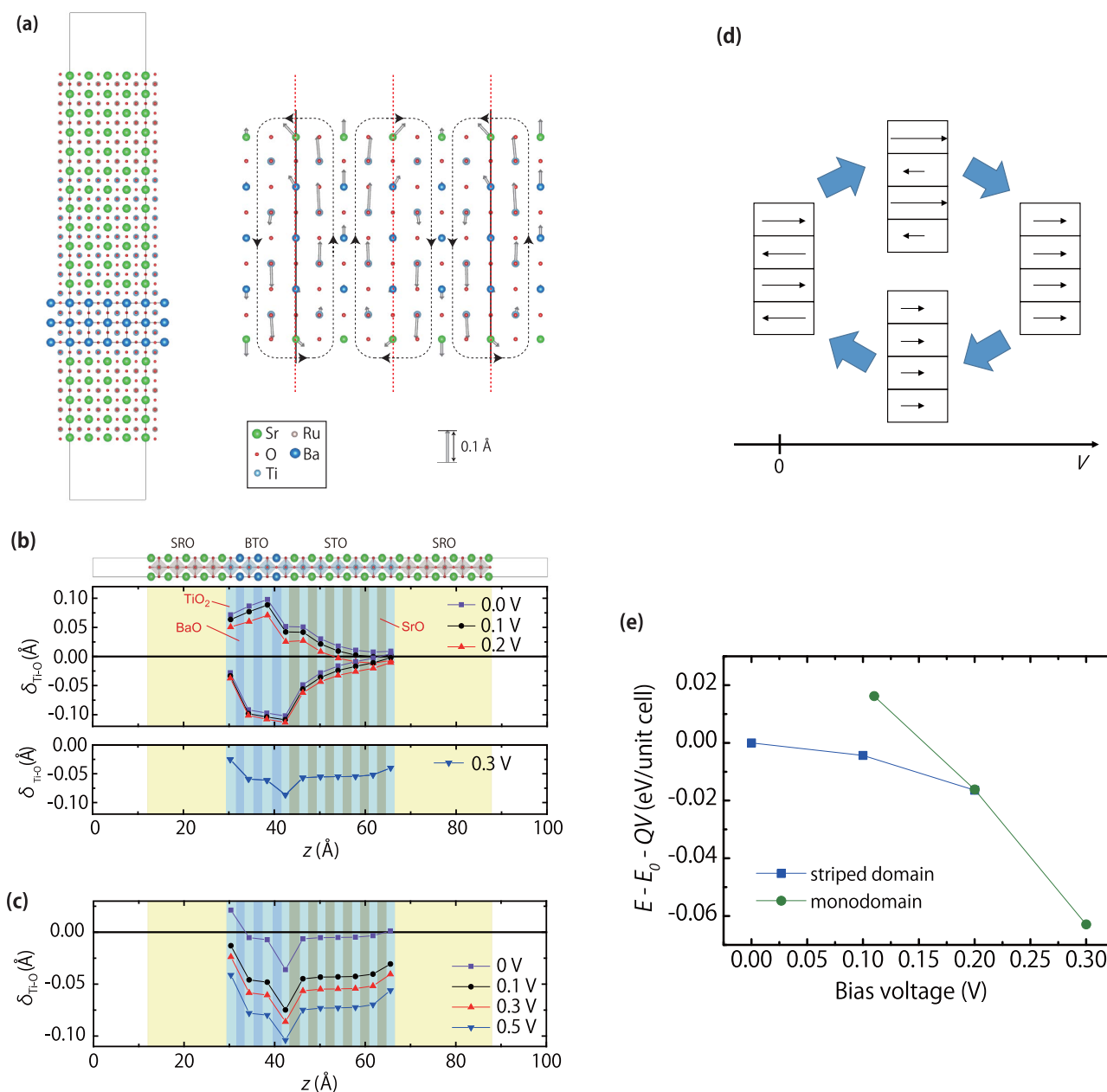


**Figure 1.** a) The  $1 \times 4$  unit cell striped-domain SRO–BTO–STO–SRO heterostructure considered in this work (left) and an enlarged view of the BTO part in the reference monodomain state with gray arrows representing the displacement of the cations when forming the striped domains (right). The length of the gray arrows is proportional to the magnitude of the displacement and can be gauged against the arrow in the lower right corresponding to a displacement of 0.1 Å. b) The evolution of the local polarization with applied bias in the striped-domain model measured by the displacement of the cations versus the anions in the TiO planes. c) The evolution of the local polarization in the monodomain-constrained model. d) Schematic of the antiferroelectric hysteresis behavior of the polarization domains in the SRO–BTO–STO–SRO capacitor. e) The calculated grand potential in the  $1 \times 4$  unit cell model in the striped-domain (blue squares) and monodomain (green circles) states.

suppression in our monodomain-constrained SRO–BTO–STO–SRO model). Calculations were also performed on the paraelectric  $(N_{\text{BTO}}, N_{\text{STO}}) = (0, 6)$  capacitor to quantify the negative capacitance effect. The in-plane lattice constants are fixed to the theoretical value for bulk cubic STO ( $a = 3.865$  Å) to simulate epitaxial growth on STO substrate, although the substrate is not considered explicitly in our model. The differential capacitance and local differential permittivity were

evaluated as described in the “Methods” section (we will refer to differential capacitance and differential permittivity simply as “capacitance” and “permittivity” hereafter). Our simulations are performed at zero temperature, but we can infer from the results a picture of the dielectric behavior near room temperature due to what may be described as error cancellation in the local density approximation employed in this work (discussion on this effect is given in the Supporting Information).

First, we examined the domain formation in the model with  $1 \times 4$  in-plane unit cells. The relaxation of the SRO layers was performed only in the direction perpendicular to the interface to suppress the  $\text{TiO}_2$  octahedral distortion<sup>[35]</sup> and simplify the analysis. The SrO layers at the SRO/BTO and SRO/STO interfaces were allowed to relax in-plane following ref. [23] which discussed ferromagnetic-like closure domains at the interface. The BTO and STO layers were allowed to relax freely. The relaxation was started with two unit cells polarized in an out-of-plane direction and the other two polarized in the opposite direction, so that the BTO part relaxed into a striped-domain structure with the  $c$ -axis aligned perpendicular to the interface. The width of each domain is two unit cells, i.e., the domain period is four unit cells. We only considered the BaO-centered striped-domain structure, as this was found to be more stable than the  $\text{TiO}_2$ -centered one in previous works.<sup>[23,36]</sup> The energy gain by domain formation in the BTO layer compared to the monodomain system was calculated to be  $\Delta E_{\text{domain}} = 47$  meV per in-plane unit cell. This compares well with the value of 30 meV reported in ref. [23] for the SRO–BTO–SRO capacitor with four BTO unit cells. This means that the zero-bias ground state, even when the BTO layer is as thin as three unit cells, is a polydomain one. A closer examination of the polarization pattern near the interfaces shows the closure pattern that was also reported in ref. [23] (Figure 1a).

Next, we turn to the bias dependence of the dielectric behavior of this striped-domain model. Figure 1b shows how the polarization in the FE/PE bilayer structure evolves with increasing bias, and we find that the bilayer capacitor exhibits a striped domain to monodomain transition at  $\approx 0.3$  V. This is in contrast to the monodomain-constrained model, which shows almost zero polarization at zero bias and whose polarization increases uniformly as bias is increased (Figure 1c). In the striped-domain model, the BTO layers are polarized in two directions at 0 V due to the formation of the striped-domain structure mentioned above. The STO layers near the interface are also polarized, implying that the screening of the depolarization field through the formation of striped domains is not perfect. As the bias is increased, the polarization in one of the domains is pushed toward zero, while the polarization in the other domain increases in magnitude. Then at 0.3 V, a transition to the monodomain structure is observed. This structure is found to be (meta)stable until the bias is decreased below 0.1 V, at which the structure returns to the striped-domain state. This hysteretic antiferroelectric-like behavior is illustrated schematically in Figure 1d. We note that similar antiferroelectric behavior was observed in a simulation of partially charge-compensated ultrathin ferroelectric films.<sup>[24]</sup> The calculated grand potential of the monodomain and polydomain states indicate that the thermodynamic transition point is at 0.2 V (Figure 1e).

The hysteresis in the capacitance and accumulated charge resulting from this antiferroelectric-like behavior is plotted in Figure 2 along with calculated capacitance values of the monodomain-constrained ( $N_{\text{BTO}}, N_{\text{STO}} = (3, 6)$ ) FE/PE bilayer capacitor and the ( $N_{\text{BTO}}, N_{\text{STO}} = (0, 6)$ ) PE capacitor. We note that the value of  $\approx 270$  fF  $\mu\text{m}^{-2}$  for the ( $N_{\text{BTO}}, N_{\text{STO}} = (0, 6)$ ) capacitor near zero bias is in good agreement with ref. [5] despite the different methodologies used for the calculations. The corresponding local potential and inverse permittivity profiles are

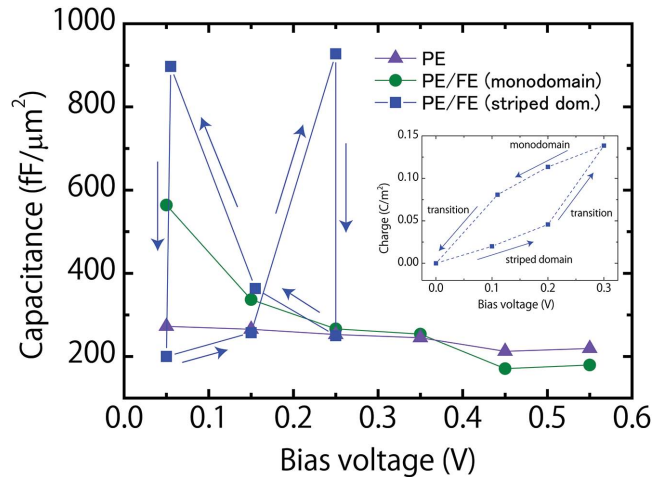


**Figure 2.** The voltage dependence of the capacitance of ( $N_{\text{BTO}}, N_{\text{STO}} = (3, 6)$ ) monodomain-constrained and multidomain FE/PE bilayer capacitors compared with the ( $N_{\text{BTO}}, N_{\text{STO}} = (0, 6)$ ) PE capacitor. Inset: the amount of charge accumulated on each of the electrode plates in the multidomain FE/PE capacitor.

shown in Figure 3a1,a2 (note that integration of the inverse differential permittivity profile corresponds directly to the inverse of the differential capacitance per unit area). Near zero bias, the FE/PE bilayer capacitor in the striped-domain state has a lower capacitance than the PE capacitor, showing that indeed, the formation of domains will limit our ability to utilize the negative capacitance. This is also clearly seen in the permittivity profile

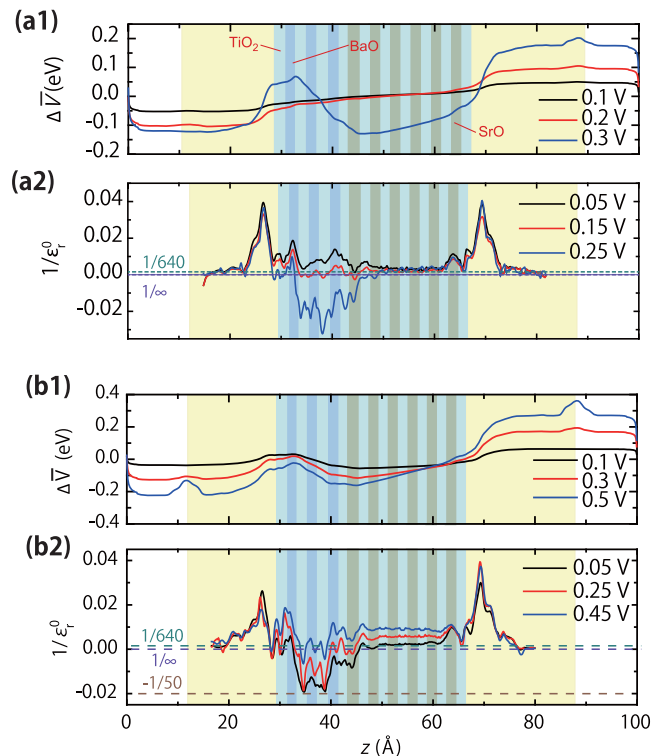


**Figure 3.** The induced potential profile and inverse permittivity profile of the striped-domain a1,a2) and monodomain-constrained b1,b2) SRO–BTO–STO–SRO capacitors as the bias is increased from 0 V.

at 0.05 V, which is nonnegative throughout the bilayer capacitor. We also note that the SRO/BTO and SRO/STO interfaces clearly show the intrinsic dead layer effect,<sup>[5]</sup> which dominates the total capacitance value since the inverse permittivity inside the BTO and STO layers is very small due to the high bulk permittivity of those materials. Between 0 and 0.2 V, applied bias pushes one of the BTO domains toward the centrosymmetric negative permittivity state, while it pushes the other domain away from the centrosymmetric state. The decrease in the inverse permittivity of the BTO part to nearly zero at 0.15 V in Figure 3a2 means that the former effect is more dominant, and the total capacitance also increases. Upon further increase of the bias, the capacitance exceeds that of the PE capacitor and shows a spike reaching over  $900 \text{ fF } \mu\text{m}^{-2}$  near 0.25 V, which corresponds to the polydomain-to-monodomain transition discussed above. The precise capacitance value would depend on the abruptness of the transition, which we are unable to quantify due to limitations in the present simulation including lack of finite-temperature effects. The field inside the BTO layers at 0.3 V clearly opposes the applied bias (Figure 3a1) and completely negates the potential drop due to the dead layer effect. The corresponding inverse permittivity profile (Figure 3a2) is negative in the BTO part, leading to the threefold capacitance boost versus the PE capacitor. This negative permittivity includes effects from the polydomain–monodomain transition itself, as well as the negative permittivity of near-centrosymmetric BTO. Once in the monodomain regime, the capacitance values and the polarization are virtually the same as those calculated in the monodomain-constrained FE/PE bilayer capacitor, which we will discuss below. This monodomain structure returns to the striped-domain structure below 0.1 V with a corresponding spike in the capacitance.

The capacitance of the monodomain-constrained bilayer capacitor is largest at zero bias and declines monotonically with increasing bias. The value of  $560 \text{ fF } \mu\text{m}^{-2}$ , which amounts to a twofold increase compared to the PE capacitor, is obtained at 0.05 V. This capacitance boost versus the PE capacitor is due to the negative permittivity of the near-centrosymmetric BTO (Figure 3b1,b2). The value of the permittivity inside the BTO layers is  $\approx -50$  as in ref. [18]. As the bias is increased, the polarization increases and the inverse permittivity of the BTO layers increases from negative to positive values. At the same time, the permittivity of the STO layers also decreases (the inverse permittivity increases) due to increasing internal field,<sup>[37]</sup> and the capacitance of the monodomain PE/FE bilayer capacitor falls below that of the PE capacitor at  $V > 0.3 \text{ V}$  (note that the total inverse capacitance is determined from the sum of the inverse capacitances of each component).

The above results can be summarized as follows. Near zero bias, the ground state is the striped-domain structure and thus the ferroelectric negative capacitance cannot be utilized. However, the monodomain state becomes stable at higher biases and remains metastable until the bias is lowered below 0.1 V. Thus, the negative permittivity of depolarized BTO can be utilized if the bias is maintained above 0.1 V after “preannealing” at higher than 0.3 V. However, the capacitance amplification due to depolarized near-centrosymmetric BTO is effective only below 0.3 V due to “too much” polarization at higher biases that pushes the ferroelectric system out of the negative permittivity

regime. One may also make use of the huge capacitance originating from the polydomain/monodomain transition if the capacitor is used as a switch between 0 V (where the system is in a polydomain state) and 0.3 V (where the system is in a monodomain state regardless of the voltage history); however, this may not be optimal in minimizing energy consumption for nanoelectronics applications since hysteresis implies energy dissipation.<sup>[38]</sup> We also point out that the specific voltages at which the switching occurs should be controllable by adopting different stack configurations. For example, it should be expected that by using electrodes with different work functions, there will be finite electric field in the stack at zero external bias (short-circuit condition). This should lead to a shift in the  $V$ -axis of Figure 2; however, the amount of shift is difficult to predict because the interfacial dead layer effect depends on the material combinations and processing conditions (some insight can be gained from first-principles simulation.<sup>[18]</sup> We also point out that the transition between higher-capacitance and lower-capacitance domain states under finite bias is a general phenomenon. This is because the grand potential  $E - E_0 - QV \approx -1/2CV^2$ , so that the higher-capacitance state will become more stable as bias is increased even if it is less stable at zero bias (see Figure 1e). The critical bias would depend on the difference in the capacitance and the domain formation energy between the domain structures, which in turn depend on the material combinations, boundary effects, and the film thickness.

We also note that the actual transition may occur at closer to the thermodynamical transition voltage, that is, the hysteresis may not be as pronounced as shown here. This is inferred because we have observed the transition through structural relaxation, which means that there is no thermal energy in the simulation to overcome energy barriers between polydomain and monodomain regimes. In realistic situations, thermal motion should assist in overcoming the barrier. Moreover, the transition would be initialized by nucleation, i.e., the lateral movement of the domain walls leading to growth in domain size. In this work, the domain width is only two perovskite unit cells wide, meaning that the smallest unit of domain wall motion leads immediately to the polydomain–monodomain transition that we have observed. This is not far off from the experimentally observed domain width of as small as three unit cells in ultrathin (three unit cells thick)  $\text{PbTiO}_3$ ,<sup>[21]</sup> and in that regard, our results are very close to what would be expected to occur in experiment. Moreover, this lower bound in domain size has been argued to be due to the  $c(2 \times 2)$  reconstruction of PTO (100) surface,<sup>[21]</sup> which does not occur in BTO. In fact, density functional theory predicts that two- and three-unit-cell domains are comparable in energy in ultrathin BTO.<sup>[23]</sup> Generally, it is expected that the domain size (in this case width) will increase with increasing ferroelectric film thickness.<sup>[27]</sup> However, in the practical application of these type of materials in nanoscale devices, such as DRAM with design rule = 10 nm, the allowed film thickness is actually very small (only a few nm), meaning that the present calculation might represent a circumstance closer to actual application. In a broader context, however, the domain size is known to vary depending not only on film thickness, but also on materials combinations and electrical boundary conditions, and the critical voltage for the transition would depend on the domain size. These points cannot

be taken into account due to the size of the calculation cell in the present work and are subjects of future study. We note, however, that the enhancement of capacitance due to domain motion suggested in previous works<sup>[12,29,32,33]</sup> is captured at least to some extent in our work, since domain motion is essentially local polarization reversal, and that is what is observed at the polydomain–monodomain transition. The magnitude of the effect may certainly be underestimated, since the resulting monodomain state has a smaller polarization than the fully polarized polydomain ferroelectric state.

Regarding nonidealities in experiment, there are also many possible sources of polarization that we have not taken into account such as defects and finite-size edge effects of the metal electrodes. Due to the versatility of ferroelectric materials in providing electrostatic screening (due to large polarization plus the formation of polarization domains), we expect that such nonidealities will be screened within a small enough distance so that our results are valid in all but the most extreme cases. Especially in the context of applying this intriguing effect to DRAM, the nonuniformity of the electric field by the electrode edge effect should be minimal. This is because in DRAM cell structure, the electrodes cover 100% of the surface area of the dielectric (see, e.g., ref. [1]), so there is no edge effect. It is of note that the trench-like structure of DRAM capacitors can induce nonuniform field effects especially at the top corner, but the top corner covers less than 5% of the capacitor area. Therefore, we can safely assume that the field nonuniformity is not a severe issue for actual application in nanoscale DRAMs.

There has been some debate over recent years whether the ferroelectric negative capacitance would be usable in actual devices. One criticism of the original idea<sup>[8]</sup> is that various screening mechanisms such as multidomain ferroelectricity would severely limit the stabilization of the negative energy curvature regime that would give rise to negative capacitance.<sup>[25,39]</sup> On the other hand, experiments on the PE/FE bilayer capacitor indicated that there indeed is a negative capacitance effect, although the mechanism was not clarified. The present calculations reconfirm that domain formation indeed limits the onset of negative capacitance at zero bias. However, in contrast to previous theoretical works such as ref. [25] which only considered the linear response near zero gate bias, our fully bias-dependent simulations show that domain dynamics and the negative energy curvature can both contribute to the negative capacitance. We predict that polarization reversal at not-too-high biases would result in the system switching to the monodomain negative capacitance regime, and that the polarization reversal itself will also be a source of the capacitance enhancement. The amount of capacitance enhancement as well as the associated hysteresis will depend on nonidealities not taken into account in the present work such as finite-temperature effects, defects, and nucleation, and further theoretical and experimental works will be necessary to clarify such points.

## Methods Section

The calculations were performed on SGI Altix 3800EX system at Institute for Solid State Physics, the University of Tokyo. Figures of atomic structures were created using VESTA

visualization software.<sup>[40]</sup> The calculations presented above were performed within the local density approximation of density functional theory using the Vienna ab initio Simulation Package (VASP).<sup>[41]</sup> VASP was modified to implement the orbital-separation approach for simulating metal/insulator/metal slabs under bias voltage.<sup>[34,41]</sup> The projector-augmented wave method was used for treating electron–ion interactions.<sup>[42]</sup> For the monodomain simulations, a  $6 \times 6 \times 1$  Monkhorst–Pack mesh was employed for  $k$ -point sampling with a Gaussian smearing of 0.05 eV. A plane wave energy cutoff of 500 eV was used for the wave function expansion. The calculations were performed under the periodic boundary condition on metal/insulator/metal slabs discussed in the main text. To simulate an isolated capacitor, the dipole–dipole interaction between adjacent unit cells were removed using the dipole correction formula<sup>[43]</sup> implemented in VASP. The out-of-plane ionic positions were fully relaxed under various bias voltages until forces on each ion were below  $1 \text{ meV } \text{Å}^{-1}$ . The differential capacitance per unit area was then evaluated as:

$$\frac{C(V)}{A} = \frac{1}{V} \frac{dE(V)}{dV} \quad (1)$$

using centered differences, where  $V$  is the applied bias and  $E$  is the energy per unit area of the capacitor.<sup>[34]</sup> The local inverse differential permittivity between the center of the electrodes was evaluated as:

$$\frac{1}{\epsilon_r(z, V)} = -\frac{\epsilon_0 A}{C(V)} \frac{\partial^2 [\Delta \bar{V}_H(z, V)]}{\partial V \partial z} \quad (2)$$

where  $\epsilon_0$  is the vacuum permittivity and  $\Delta \bar{V}_H(z, V)$  is the macroscopically averaged induced potential profile under bias  $V$  (a derivation is given in the Supporting Information).

The polydomain simulations were performed using an  $8 \times 2 \times 1$  Monkhorst–Pack  $k$ -point mesh with a Gaussian smearing of 0.05 eV. A plane wave energy cutoff of 400 eV was used for the wave function expansion. The structural relaxation was performed until the forces on each atom were below  $1 \text{ meV } \text{Å}^{-1}$ . The capacitance was evaluated from the voltage-dependence of the free charge  $dQ/dV$ , where the free charge  $Q$  was calculated using the method of ref. [44]

## Supporting Information

Supporting Information is available from the Wiley Online Library or from the author.

## Acknowledgements

This work was supported by the Global COE Program “Global Center of Excellence for Mechanical Systems Innovation” and by Asian Core Program by Japan Society for the Promotion of Science (JSPS). It was also supported by Grant-in-Aid for Scientific Research on Innovative Areas, “Materials Design through Computics (2203)” (No. 20104007) and for Scientific Research (B) (No. 20360016) by the Ministry of Education, Culture, Science, and Technology (MEXT) of Japan. S.K. is supported by Grant-in-Aid for Young Scientists (B) (No. 15K20953)

by JSPS. S.H. was supported by Pioneer Research Center Program (2012-0009563), and C.S.H. was supported by the Global Research Laboratory program (2012040157) through the National Research Foundation (NRF) of Korea.

Received: June 17, 2015

Revised: October 1, 2015

Published online: November 16, 2015

- [1] S. K. Kim, S. W. Lee, J. H. Han, B. Lee, S. Han, C. S. Hwang, *Adv. Funct. Mater.* **2010**, *20*, 2989.
- [2] C. A. Mead, *Phys. Rev. Lett.* **1961**, *6*, 545.
- [3] C. S. Hwang, *J. Appl. Phys.* **2002**, *92*, 432.
- [4] J. Swerts, M. Popovici, B. Kaczer, M. Aoulaiche, A. Redolfi, S. Clima, C. Caillat, W. C. Wang, V. V. Afanasev, N. Jourdan, C. Olk, H. Hody, S. Van Elshocht, M. Jurczak, *IEEE Electron Device Lett.* **2014**, *35*, 753.
- [5] M. Stengel, N. A. Spaldin, *Nature* **2006**, *443*, 679.
- [6] R. Plonka, R. Dittmann, N. A. Pertsev, E. Vasco, R. Waser, *Appl. Phys. Lett.* **2005**, *86*, 202908.
- [7] S. Schmelzer, D. Bräuhäus, S. Hoffmann-Eifert, P. Meuffels, U. Böttger, L. Oberbeck, P. Reinig, U. Schröder, R. Waser, *Appl. Phys. Lett.* **2010**, *97*, 132907.
- [8] S. Salahuddin, S. Datta, *Nano Lett.* **2008**, *8*, 405.
- [9] V. V. Zhirnov, R. K. Cavin, *Nat. Nanotechnol.* **2008**, *3*, 77.
- [10] T. Kopp, J. Mannhart, *J. Appl. Phys.* **2009**, *106*, 064504.
- [11] L. Li, C. Richter, S. Paetel, T. Kopp, J. Mannhart, R. C. Ashoori, *Science* **2011**, *332*, 825.
- [12] A. I. Khan, D. Bhowmik, P. Yu, S. J. Kim, X. Pan, R. Ramesh, S. Salahuddin, *Appl. Phys. Lett.* **2011**, *99*, 113501.
- [13] G. A. Salvatore, A. Rusu, A. M. Ionescu, *Appl. Phys. Lett.* **2012**, *100*, 163504.
- [14] W. Gao, A. Khan, X. Marti, C. Nelson, C. Serrao, J. Ravichandran, R. Ramesh, S. Salahuddin, *Nano Lett.* **2014**, *14*, 5814.
- [15] A. I. Khan, K. Chatterjee, B. Wang, S. Drapcho, L. You, C. Serrao, S. R. Bakaul, R. Ramesh, S. Salahuddin, *Nat. Mater.* **2015**, *14*, 182.
- [16] D. J. R. Appleby, N. K. Ponon, K. S. K. Kwa, B. Zou, P. K. Petrov, T. Wang, N. M. Alford, A. O'Neill, *Nano Lett.* **2014**, *14*, 3864.
- [17] J. Junquera, P. Ghosez, *Nature* **2003**, *422*, 506.
- [18] M. Stengel, D. Vanderbilt, N. A. Spaldin, *Nat. Mater.* **2009**, *8*, 392.
- [19] C. Kittel, *Phys. Rev.* **1946**, *70*, 965.
- [20] E. V. Chenskii, V. V. Tarasenko, *J. Exp. Theor. Phys.* **1982**, *56*, 618.
- [21] D. D. Fong, G. B. Stephenson, S. K. Streiffer, J. A. Eastman, O. Auciello, P. H. Fuoss, C. Thompson, *Science* **2004**, *304*, 1650.
- [22] T. Nishimatsu, U. Waghmare, Y. Kawazoe, D. Vanderbilt, *Phys. Rev. B* **2008**, *78*, 104104.
- [23] P. Aguado-Puente, J. Junquera, *Phys. Rev. Lett.* **2008**, *100*, 177601.
- [24] E. Glazkova, K. McCash, C.-M. Chang, B. K. Mani, I. Ponomareva, *Appl. Phys. Lett.* **2014**, *104*, 012909.
- [25] A. Cano, D. Jiménez, *Appl. Phys. Lett.* **2010**, *97*, 133509.
- [26] D. D. Fong, A. M. Kolpak, J. A. Eastman, S. K. Streiffer, P. H. Fuoss, G. B. Stephenson, C. Thompson, D. M. Kim, K. J. Choi, C. B. Eom, I. Grinberg, A. M. Rappe, *Phys. Rev. Lett.* **2006**, *96*, 127601.
- [27] V. A. Stephanovich, I. A. Luk'yanchuk, M. G. Karkut, *Phys. Rev. Lett.* **2005**, *94*, 047601.
- [28] M. Dawber, N. Stucki, C. Lichtensteiger, S. Gariglio, P. Ghosez, J.-M. Triscone, *Adv. Mater.* **2007**, *19*, 4153.
- [29] P. Zubko, N. Stucki, C. Lichtensteiger, J.-M. Triscone, *Phys. Rev. Lett.* **2010**, *104*, 187601.
- [30] Y. S. Kim, D. H. Kim, J. D. Kim, Y. J. Chang, T. W. Noh, J. H. Kong, K. Char, Y. D. Park, S. D. Bu, J.-G. Yoon, J.-S. Chung, *Appl. Phys. Lett.* **2005**, *86*, 102907.
- [31] C.-L. Jia, V. Nagarajan, J.-Q. He, L. Houben, T. Zhao, R. Ramesh, K. Urban, R. Waser, *Nat. Mater.* **2007**, *6*, 64.
- [32] A. M. Bratkovsky, A. P. Levanyuk, *Phys. Rev. B* **2001**, *63*, 132103.
- [33] A. M. Bratkovsky, A. P. Levanyuk, *Appl. Phys. Lett.* **2006**, *89*, 253108.
- [34] S. Kasamatsu, S. Watanabe, S. Han, *Phys. Rev. B* **2011**, *84*, 085120.
- [35] A. T. Zayak, X. Huang, J. B. Neaton, K. M. Rabe, *Phys. Rev. B* **2006**, *74*, 094104.
- [36] J. Padilla, W. Zhong, D. Vanderbilt, *Phys. Rev. B* **1996**, *53*, 5969.
- [37] A. Antons, J. B. Neaton, K. M. Rabe, D. Vanderbilt, *Phys. Rev. B* **2005**, *71*, 024102.
- [38] M. H. Park, H. J. Kim, Y. J. Kim, T. Moon, K. D. Kim, C. S. Hwang, *Adv. Energy Mater.* **2014**, *4*, 1400610.
- [39] G. Catalan, D. Jiménez, A. Gruverman, *Nat. Mater.* **2015**, *14*, 137.
- [40] K. Momma, F. Izumi, *J. Appl. Crystallogr.* **2008**, *41*, 653.
- [41] G. Kresse, J. Furthmüller, *Phys. Rev. B* **1996**, *54*, 11169.
- [42] P. E. Blöchl, *Phys. Rev. B* **1994**, *50*, 17953.
- [43] L. Bengtsson, *Phys. Rev. B* **1999**, *59*, 12301.
- [44] S. Kasamatsu, S. Watanabe, S. Han, *Phys. Rev. B* **2015**, *92*, 115124.